J Mater Sci (2008) 43:6441–6452
DOI 10.1007/s10853-008-2975-5

INTERFACE SCIENCE

On interfacial velocities during abnormal grain growth at ultra-high driving forces

G. D. Hibbard · K. T. Aust · U. Erb

Received: 13 March 2008 / Accepted: 26 August 2008 / Published online: 17 September 2008

Abstract Interfacial velocities during grain growth studies of nanocrystalline materials have been investigated. Two types of interfacial velocity parameters were developed in Ni and Ni–Co alloys. The first was a transformation-averaged parameter based on the time to consume the nanocrystalline matrix by abnormal grain growth. The second was a time-averaged parameter based on the rate of size increase of the largest growing grains. Despite the ultra-high driving force and rapid loss of nanostructure during annealing, the averaged grain boundary velocities are considerably lower than reported velocities during recrystallization in high purity systems for the same homologous temperature. It was found that the time-averaged abnormal growth front velocity decreased with increasing migration distance, which was interpreted in terms of a dynamic sulfur segregation model.

Introduction

The issue of interfacial velocity has not been widely addressed in grain growth studies of nanocrystalline materials. This is perhaps surprising, considering that it is the velocity distribution of the migrating grain boundaries that ultimately controls the thermal stability and provides insight into the rate-limiting dragging forces. Grain growth in nanocrystalline Ni electrodeposits containing S-impurities has been extensively studied (e.g., [1–11]). These nanostructures undergo a complex sequence of multi-staged grain growth during isothermal annealing. There is an initial stage of abnormal grain growth [1, 2], in which a small fraction of the starting grains (on the order of 0.01%) grow into the 100–1000 nm size range. The initial abnormal growth stage is completed once the migrating abnormal growth fronts (AGFs) of the nonuniformly growing grains have impinged and consumed the otherwise stable nanocrystalline matrix [4–6]. The resulting structure has a relatively narrow grain size distribution and further growth occurs uniformly at a much slower rate [5, 6]. Eventually, however, a second stage of abnormal growth is initiated which is characterized by cuboidal shaped grains growing via the migration of planar reaction fronts that are composed of many individual grain boundary segments [6, 8]. Although the initial stage of abnormal grain growth contributes to this unusual morphology, it is beyond the scope of the present study.

The mechanisms controlling abnormal grain growth in nanocrystalline Ni are not fully understood at present. A study of abnormal grain growth in commercial grade polycrystalline Ni reported a correlation between grain boundary faceting and abnormal grain growth, which was interpreted in terms of anisotropy in the grain boundary energy [12]. For nanocrystalline Ni electrodeposits, there is a growing body of experimental evidence indicating that there is a change in crystallographic texture during the initial abnormal growth stage [9–11]. Electrodeposits with a strong (001) as-deposited fiber texture experienced a strengthening of the (111) texture during the initial (abnormal) growth stage [9]. A similar effect of decreasing (100) texture with increasing (111) texture was observed in electrodeposited nanocrystalline Ni–45%Fe [13] and has also been reported over a range of Ni–Fe alloy concentrations, e.g., from permalloy (Ni–22%Fe) [14] to invar (Ni–64%Fe) [15]. These crystallographic texture changes have generally been interpreted in terms of an orientation

G. D. Hibbard (✉) · K. T. Aust · U. Erb
Department of Materials Science and Engineering, University of Toronto, 184 College Street, Toronto, ON, Canada M5S 3E4
e-mail: glenn.hibbard@utoronto.ca

dependence of the grain boundary energy [10, 15]. However, these texture changes are not simple and their evolution depends on the annealing temperature and the starting (as-deposited) texture [9]. A recent study in nanocrystalline Ni observed that the first grown grains had a (311) texture, but that the dominant texture gradually changed to a (111) orientation with prolonged annealing [11].

It is the initial loss of nanostructure by abnormal grain growth that has the greatest technological significance and it can occur quickly; at 693 K the nanocrystalline Ni matrix is consumed in less than 30 s [6]. An in-situ transmission electron microscopy (TEM) annealing study of electrodeposited nanocrystalline Ni [7] showed that migration of the AGFs occurred in discontinuous steps over limited sections of the reaction front. Nanocrystalline Ni–Co alloys exhibit a similar overall type of nonuniform grain growth and can have a relatively broad range of thermal stability [16]. The present study examines experimental results from previous ex-situ TEM annealing studies in Ni and Ni–Co alloys by the same authors [4–7, 16] to investigate two issues of grain boundary velocity in nanocrystalline materials. First, an overall transformation-averaged AGF velocity, based on the time to consume the nanocrystalline matrix, was determined to examine the effect of annealing temperature and electrodeposit thermal stability. Second, the time-averaged AGF velocity for the most rapidly growing size class of grains was measured as a function of grain size. This approach provides unique insights into the nature of the rate controlling mechanisms during grain growth in nanocrystalline electrodeposits.

Experimental

Nanocrystalline Ni and Ni–Co alloys (Ni–37%Co, Ni–52%Co, and Ni–74%Co) were synthesized by pulse current electrodeposition [17, 18]. Samples were electrodeposited onto Ti cathodes and subsequently mechanically stripped from the substrate to produce free-standing sheets. The starting microstructure of each electrodeposit was extensively characterized by X-ray diffraction (XRD), transmission electron microscopy (TEM), and infra-red (IR) spectroscopy—microstructural characterization summarized in Table 1. Details on the microstructural characterization of the Ni [4–7] and Ni–Co [16] electrodeposits are reported elsewhere. Each electrodeposit exhibited a uniform and equiaxed microstructure. Grain size distribution parameters of the starting microstructure (mean, d_0, range, r_0, and standard deviation, s_0) were determined by measuring the size of more than 250 grains from dark field TEM micrographs; the as-plated electrodeposits had mean grain sizes of 20 nm (Ni) and 12 nm (Ni–Co alloys). The Ni, Ni–37%Co, and Ni–52%Co deposits all had the α(FCC) crystal structure, while the Ni–74%Co electrodeposit had a two phase α + ε (HCP) structure. The sulfur and carbon impurity concentration in each electrodeposit was measured by IR spectroscopy; sulfur values ranged from 190 to 850 ppm (by weight) and carbon values ranged from 220 to 680 ppm, which are typical values for nanocrystalline electrodeposits produced from saccharin containing electrolytes [19].

Table 1 Microstructural characterization summary of the as-deposited structures: mean grain size, d_0, range, r_0, and standard deviation s_0; sulfur concentration [S], and carbon concentration [C] (both alloy and impurity concentrations specified by weight)

Sample	d_0 (nm)	r_0 (nm)	s_0 (nm)	[S] (ppm)	[C] (ppm)
n-Ni	20	<5–50	9.1	850	350
n-Ni–37%Co	12	<5–36	5.4	190	220
n-Ni–52%Co	12	<5–42	6.0	340	450
n-Ni–74%Co	12	<5–38	5.8	550	680

Average interfacial velocities were determined by measuring the size increase of the abnormally growing grains. Samples were annealed in a salt bath and subsequently thinned to electron transparency for TEM characterization. The effect of temperature on the average grain boundary velocity was determined by isothermally annealing samples from the nanocrystalline Ni electrodeposit at 493 K for times ranging from 600 s to 8.64×10^5 s; at 593 K for times ranging from ~1 s to 3.96×10^4 s; and at 693 K for times ranging from <1 s to 3.6×10^3 s. The effect of increasing the thermal stability by alloying on the average grain boundary velocity was examined in nanocrystalline Ni–37%Co, Ni–52%Co, and Ni–74%Co; samples were annealed at a constant temperature of 573 K for times ranging from 10 s to 3.6×10^4 s. The present study examined these annealed microstructures to determine several simple interfacial velocity parameters for nanocrystalline electrodeposits. Dark field TEM provided a means for obtaining the relative number fraction of nanocrystalline matrix grains and abnormally growing grains based on crystallographic orientation with respect to the electron beam [4, 5]. Bright field TEM provided imaging of significantly more grains and was used to estimate the size of the largest annealed grains.

Results and discussion

Transformation-averaged interfacial velocity

Equivalent transformed microstructures were needed to meaningfully compare interfacial migration rates at different temperatures and in different alloy systems. The simplest measure is the change in mean grain size, Δd, from the as-deposited to the 'fully' annealed microstructure at the end of abnormal grain growth (i.e., at the point when the nanocrystalline matrix has been completely consumed by abnormal grain growth). Experimentally measuring this parameter is made easier by the fact that the rate of further grain growth decreases by a factor of $\sim 10^2$ once the nanocrystalline matrix has been consumed and the growth mechanism changes from abnormal to normal grain growth [4–6]. For example, isothermal annealing of nanocrystalline Ni at 593 K for 1 h resulted in a mean grain size increase from 20 to 350 nm, at which point the nanocrystalline matrix had been completely consumed and a slower normal grain growth stage had begun. During the next 10 h of continuing normal grain growth, the mean grain size only increased by an additional $\sim$50 nm [4–6]. In addition, there was no significant difference between the grain size ($\sim$350 nm) just after complete consumption of the nanocrystalline Ni matrix for samples annealed at 493, 593, and 693 K, suggesting that there was comparatively little effect of temperature on the density of abnormally growing grains over the 200 K annealing window studied.

Table 2 Summary of average abnormal growth front velocity parameters: annealing temperature (T); bracketing annealing times for incomplete (t_i) and complete (t_c) consumption of the nanocrystalline matrix; and corresponding upper ($v_\mathrm{trans}^\mathrm{upper}$) and lower ($v_\mathrm{trans}^\mathrm{lower}$) velocity estimates

System	T (K)	t_i (s)	t_c (s)	$v_\mathrm{trans}^\mathrm{upper}$ (nm/s)	$v_\mathrm{trans}^\mathrm{lower}$ (nm/s)
n-Ni	493	4.32×10^5	8.64×10^5	3.8×10^{-4}	1.9×10^{-4}
n-Ni	593	1.8×10^3	3.6×10^3	9.2×10^{-2}	4.6×10^{-2}
n-Ni	693	5	30	33	5.5
n-Ni–37%Co	573	60	120	3.1	1.5
n-Ni–52%Co	573	600	3.6×10^3	0.28	4.7×10^{-2}
n-Ni–74%Co	573	7.2×10^3	3.6×10^4	2.7×10^{-2}	5.4×10^{-3}

In contrast to the size increase, it is more difficult to measure the length of time required to consume the nanocrystalline matrix. However, it is possible to bracket the end point of abnormal grain growth by using annealing times that result in incomplete (Δt_i) and complete (Δt_c) consumption of the nanocrystalline matrix. For example, Fig. 1 presents bright field TEM images of nanocrystalline Ni annealed for 5 s (Fig. 1a) and 30 s (Fig. 1b) at 693 K, corresponding to just before and just after the complete consumption of the nanocrystalline matrix. At lower temperatures, the annealing time required to fully consume the nanocrystalline matrix was found to increase from between 1.8×10^3 and 3.6×10^3 s at 593 K and from between 4.32×10^5 s and 8.64×10^5 s at 493 K [6], Table 2. A transformation-averaged interfacial velocity based on the mean grain size increase can be obtained using the bracketing time intervals as:

$$v_\mathrm{trans} = \frac{\Delta d}{2\Delta t} \tag{1}$$

Values are summarized for the three isothermal annealing temperatures in Table 2. This parameter is effectively a global kinetic average over all of the growing grains and over the full transformation time, making it relevant to the kinetic parameters measured by differential scanning calorimetry (DSC), as will be discussed below. Note that while it is difficult to extract the volume fraction transformed from a continuous range of annealed grain sizes, an estimate can be taken from the measured grain size distributions by using the largest grain

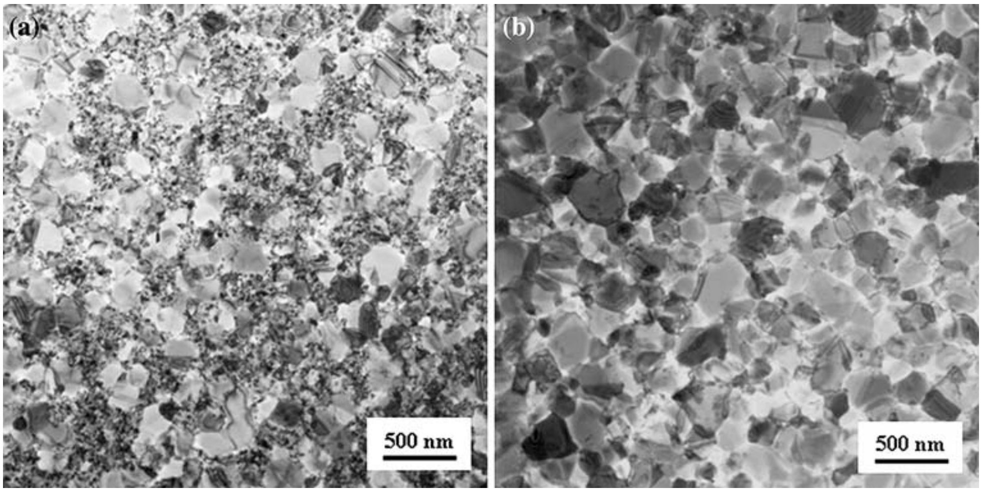

Fig. 1 Bright field TEM images of nanocrystalline Ni annealed at 693 K for 5 s (**a**) and 30 s (**b**), showing the transformed microstructures just before and after complete consumption of the nanocrystalline matrix

size from the starting nanostructure as the transformation threshold (i.e., $\sim$50 nm for Ni, Table 1). Using this approach, the lower time estimates of 4.32×10^5 s at 493 K, 1.8×10^3 s at 593 K, and 5 s at 693 K correspond to volume fractions transformed of $\sim$0.94, $\sim$0.97, and $\sim$0.93.

As would be expected, the transformation-averaged velocities for nanocrystalline Ni strongly depend on the isothermal annealing temperature, between 3.8×10^{-4} and 1.9×10^{-4} nm/s at 493 K and between 33 and 5.5 nm/s at 693 K. Upper and lower average velocities are shown in Fig. 2 in the form of an Arrhenius plot (i.e., natural logarithm of rate as a function of inverse absolute temperature). Samples from the same nanocrystalline Ni electrodeposit were previously studied by DSC [4]; an activation energy for abnormal grain growth ($Q = 1.46$ eV) was obtained by annealing samples at multiple heating rates (0.083–1.33 K/s) and measuring the shift in peak temperature with increasing scanning rate, using a modified Kissinger analysis [20]. This activation energy is shown in Fig. 2 as a line of slope $-Q/k_B$ where k_B is the Boltzmann constant. Figure 2 shows that the relative increase in transformation-averaged interfacial velocity by TEM characterization of ex-situ annealed electrodeposits is consistent with the activation energy of abnormal grain growth measured by DSC.

The effect of electrodeposit thermal stability due to alloying on v_{trans} was studied in the Ni–Co alloys by bracketing the annealing time required to completely consume the nanocrystalline matrix at 573 K. The Ni–37%Co electrodeposit had the lowest thermal stability; only 60–120 s were required to consume the nanocrystalline matrix. In contrast it took between 7.2×10^3 and 3.6×10^4 s to consume the nanocrystalline matrix of the Ni–74%Co electrodeposit, Table 2. The grain sizes at the end of abnormal grain growth were 380, 350, and 400 nm, leading to Δd parameters of $\sim$370, $\sim$340, and $\sim$390 nm, for the Ni–37%Co, Ni–52%Co, and Ni–74%Co electrodeposits, respectively. Upper and lower transformation-averaged interfacial velocities for the Ni–Co electrodeposits were calculated using Eq. 1 and are summarized in Table 2. Note that volume fraction transformed estimates of $\sim$0.97, $\sim$0.92, and $\sim$0.93, were obtained for the incomplete annealing times in the Ni–37%Co, Ni–52%Co, and Ni–74%Co deposits, respectively.

The nanocrystalline Ni–Co electrodeposits were also previously characterized by DSC [16]. The peak temperature, T_p, of grain growth (i.e., the temperature at which the maximum rate of transformation along the DSC scan occurs, e.g., [20]) provides a useful relative indicator for ranking the thermal stability. The transformation-averaged velocity range (defined by the upper and lower velocity limits, Table 2) at 573 K is plotted as a function of DSC peak temperature in Fig. 3 for nanocrystalline Ni–Co at the arbitrarily selected scanning rate of 0.67 K/s ($T_p = 584$, 613, and 619 K, for the Ni–37%Co, Ni–52%Co, and Ni–74%Co, respectively [16]). Note that the approximately two orders of magnitude difference between the v_{trans} parameters for the Ni–37%Co and Ni–74%Co electrodeposits span only a 35 K difference in the peak temperature of grain growth.

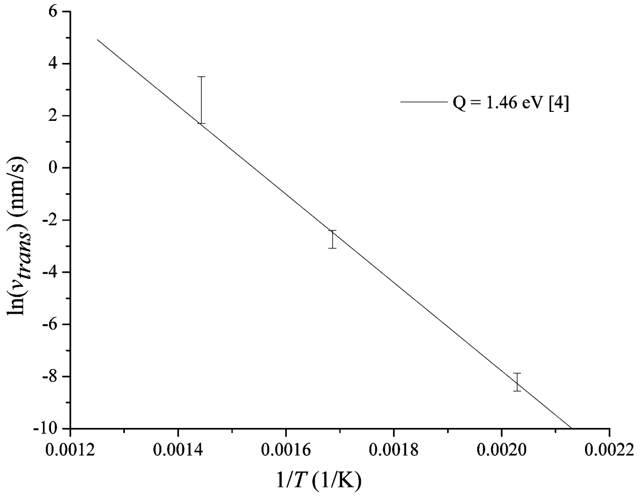

Fig. 2 Transformation-averaged interfacial velocity estimates for nanocrystalline Ni based on the mean grain size increase through abnormal grain growth (error bars denote the upper and lower bound estimates from Table 2). The *solid line* has a slope of $-Q/k_B$, where $Q = 1.46$ eV is the activation energy of grain growth for the same electrodeposit determined by differential scanning calorimetry [4] and k_B is the Boltzmann constant

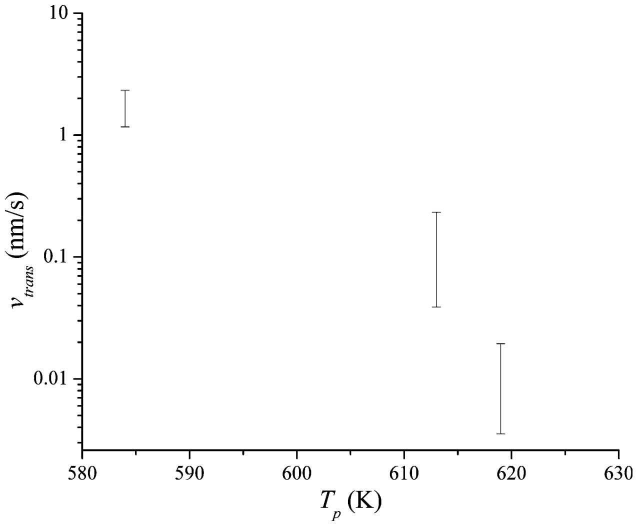

Fig. 3 Transformation-averaged (v_{trans}) interfacial velocities for nanocrystalline Ni–Co alloys at 573 K as a function of the peak temperature (T_p) of grain growth obtained from differential scanning calorimetry at a scanning rate of 0.67 K s^{-1} [16]. Note that the error bars denote the upper and lower bound estimates from Table 2

Time-averaged AGF velocities

Figure 4a presents a grain size distribution obtained from dark field TEM images of nanocrystalline Ni annealed at 493 K for 4.32×10^5 s, corresponding to a volume fraction transformed of $\sim$0.94. Overall, the grain sizes range from <5 nm to $\sim$800 nm out of a total sampling of $\sim$500 grains. However, no measurable size increase was seen for the majority of the grains. This can be more clearly seen in Fig. 4b where the grain size distribution is plotted over the 0–100 nm size range. Also shown in Fig. 4b are the grain size distributions over the same size range from the starting nanostructure and after 600 s of annealing at 493 K (i.e., corresponding to a volume fraction transformed of $\sim$0.1). There was no measurable shift in the position of the modal peak with increasing annealing time. This suggests that the curvature-based driving force for AGF migration is not decreasing until impingement with other abnormally growing grains occurs.

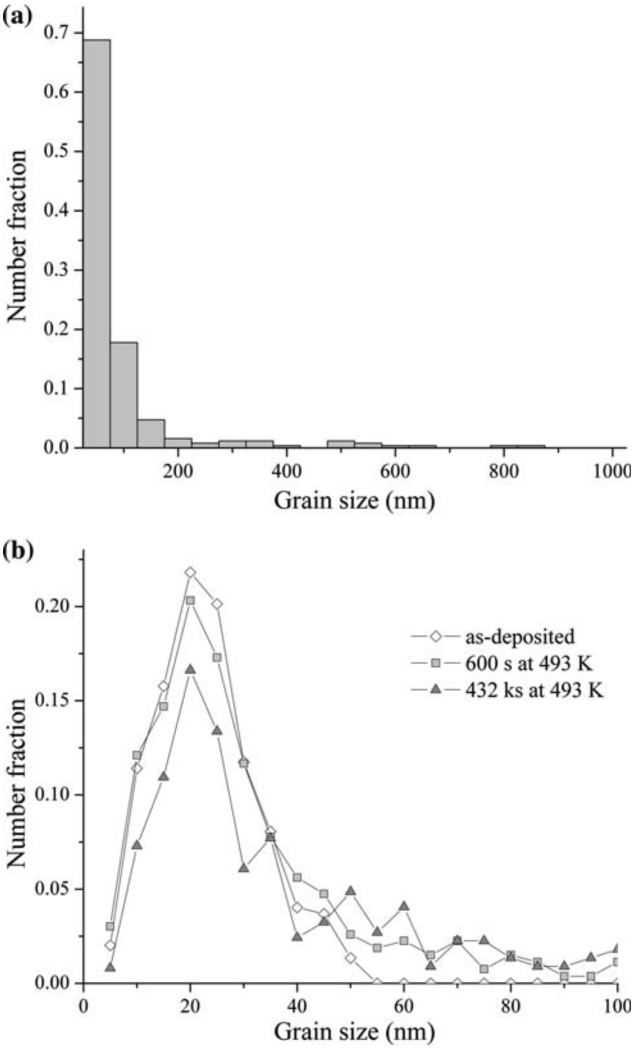

Fig. 4 Grain size distribution (full scale (**a**) and <100 nm size range (**b**)) for nanocrystalline Ni after annealing at 493 K for 4.32×10^5 s (sample size $\sim$500 grains). Also shown in (**b**) are the grain size distributions for the as-deposited nanostructure and after 600 s of annealing at 493 K

Further insight into the AGF velocity can be obtained by examining the time-averaged velocity of the largest abnormally grown grains. The right skew limit of the partially transformed grain size distribution (i.e., the size class of the largest abnormally grown grains) provides a unique reference point for linking the isothermally annealed microstructures, i.e., effectively providing an upper time-averaged limit as to how fast the AGFs can migrate through the nanocrystalline matrix. However, the right hand skew of the grain size distribution as measured from dark field TEM imaging (Fig. 4a) was sparsely populated despite the large number of grains measured (>500 per sample). To obtain a more meaningful estimate for the largest grain size class, bright field TEM imaging was used since all of the abnormally growing grains in a particular region are visible and the issue of overlapping grains becomes less and less significant for the largest grains in the annealed nanostructure.

Figure 5 presents the largest abnormal grain size class, L_x, measured from bright field TEM images for nanocrystalline Ni plotted as a function of the isothermal annealing time at 493 and 593 K. The parameter L_x was determined from the average of the ten largest grain size measurements for each annealing condition (error bars give the standard deviation). There is initially a rapid increase in the size of the largest grains, which is followed by a much slower increase through the remaining period of abnormal grain growth. This transition can be understood by considering the following. Near the end of abnormal grain growth the largest grains are surrounded either by the comparatively stable $\sim$20 nm grain size matrix or by other abnormally grown grains [5, 6]. When two migrating AGFs encounter, there is a sharp reduction in the local curvature, causing a substantial local decrease in the driving force for further migration.

Simple estimates for the time-averaged AGF velocities can be obtained from the right skew limit of the grain size distributions. In one approach, the velocity v_{AGF} is obtained by tracing the largest grain size, L_x, obtained at annealing time t_x back to the previously annealed nanostructure, L_{x-1} obtained at t_{x-1} as:

$$v_{\mathrm{AGF}} = \frac{L_x - L_{x-1}}{2(t_x - t_{x-1})}. \tag{2}$$

Figure 6 presents v_{AGF} estimates for nanocrystalline Ni as a function of annealing time at 493 and 593 K. At both temperatures, the time-averaged AGF velocity rapidly decreases with increasing annealing time. The most significant reduction occurs during the earliest stages of abnormal grain growth. For example, at 493 K the largest grain size class increases from 50 to 135 nm after 600 s,

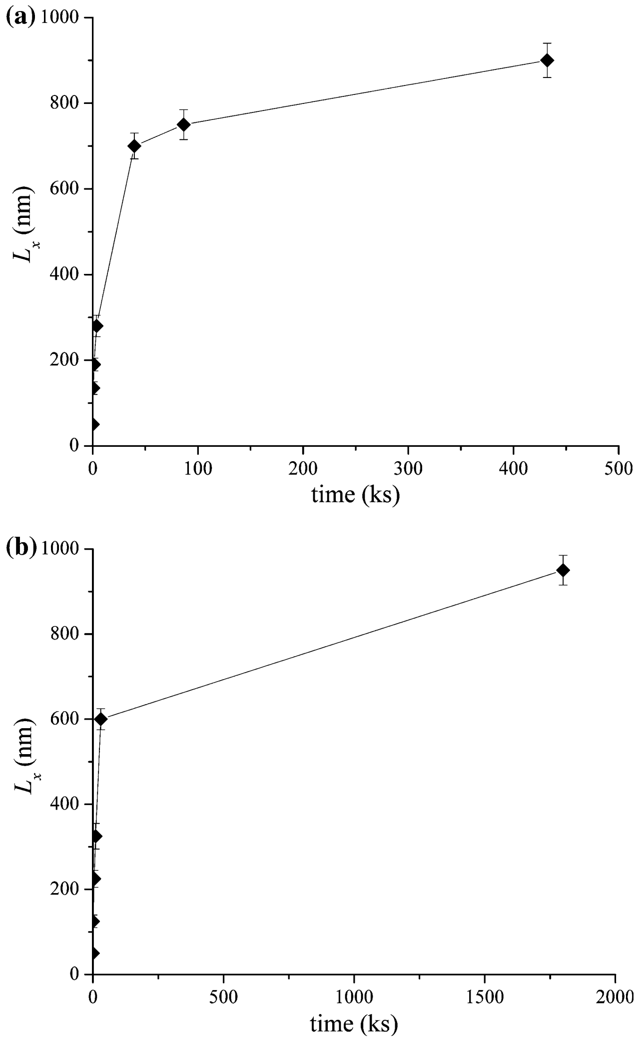

Fig. 5 Largest abnormally grown grain size class, L_x, as a function of isothermal annealing time in nanocrystalline Ni at 493 K (**a**) and 593 K (**b**)

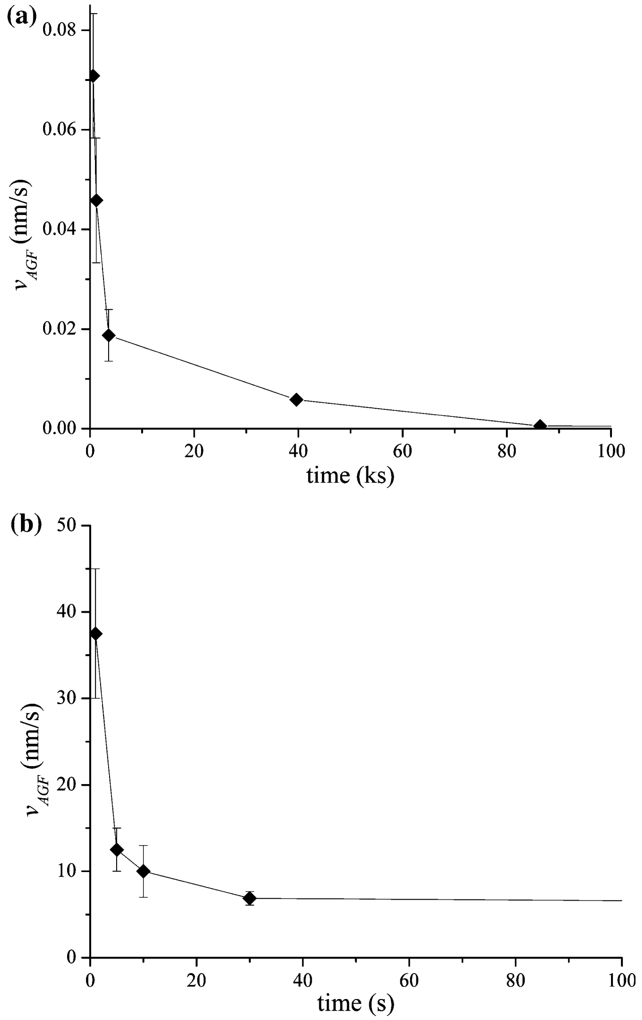

Fig. 6 Time-averaged abnormal growth front velocity (v_{AGF}) as a function of isothermal annealing time in nanocrystalline Ni during the early stages of abnormal grain growth at 493 K (**a**) and 593 K (**b**)

corresponding to $v_{\mathrm{AGF}} = 7.1 \times 10^{-2}$ nm/s. If the AGF velocity continued at this average rate, a grain size on the order of 500–600 nm would be expected after 3600 s of annealing. In fact, the largest size class after 3600 s is <300 nm (Fig. 5). This early period of nonlinear grain size increase is occurring before significant AGF impingement limits the size of the largest grains. This can be seen in Fig. 7 where bright field TEM images of typical abnormally grown grains in the largest size class for annealing times of 600, 1200, and 3600 s at 493 K are shown. At these earliest points, the largest abnormally growing grains are generally entirely surrounded by nanocrystalline matrix—i.e., before impingement of adjacently growing grains lowers the migration rate and the overall volume fraction transformed is still comparatively low (i.e., ~0.2 after 3600 s at 493 K).

The time-averaged AGF velocity of the largest size class was also measured in the Ni–Co alloys. Samples were annealed at 573 K for times ranging from 10 s to 3.6×10^4 s. The largest abnormal grain sizes were measured from bright field TEM micrographs and are plotted as a function of annealing time in Fig. 8. There is a significant difference in the rate of largest grain size increase between the three electrodeposits. For example, after 30 s of annealing at 573 K the largest grain sizes are 800, 300, and 65 nm for the Ni–37%Co, Ni–52%Co, and Ni–74%Co electrodeposits, respectively. However, the overall shape of the curves is approximately the same for the Ni–Co electrodeposits (Fig. 8) as for the Ni electrodeposit (Fig. 5). Time-averaged AGF velocities were also calculated for each of the Ni–Co electrodeposits and are plotted as a function of annealing time in Fig. 9. Like the case for Ni, the largest decrease in v_{AGF} occurs during the earliest annealing time. Furthermore, in this earliest period the abnormally growing grains are again generally surrounded by stable nanocrystalline matrix [16].

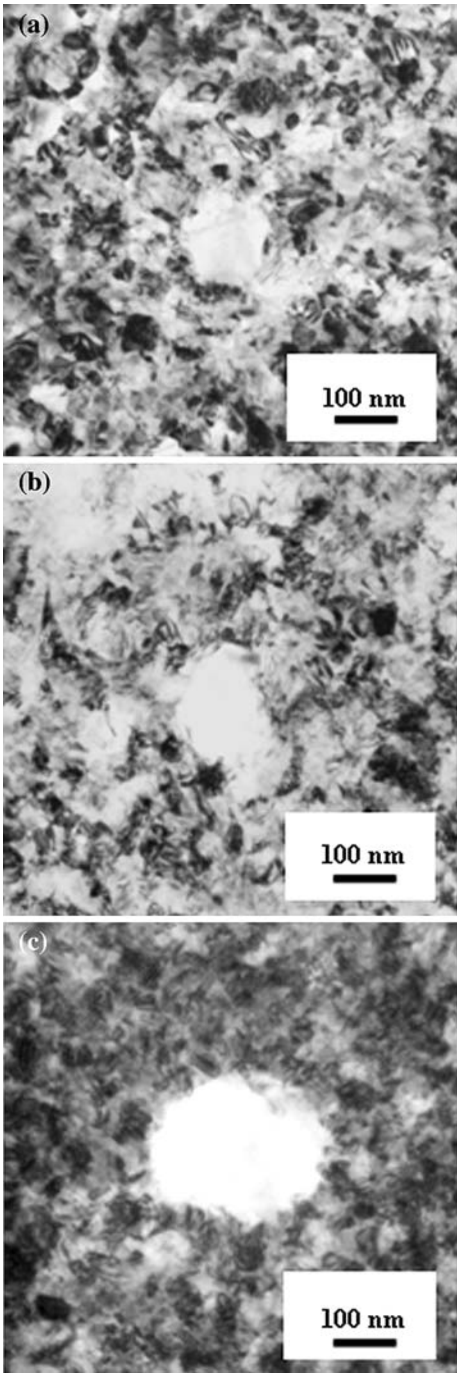

Fig. 7 Bright field TEM images showing typical abnormally grown grains in nanocrystalline Ni after isothermal annealing at 493 K for 600 s (**a**), 1200 s (**b**), and 3600 s (**c**)

Previously reported grain boundary velocities

The average interfacial velocities from the present study can be considered with respect to experimentally measured grain boundary velocities from bicrystal and recrystallization studies, see reviews in [21–23]; comparisons can be made on the basis of the driving force for grain boundary migration and the homologous annealing temperature. Homologous temperatures for the isothermal annealing experiments in Ni ($T_m = 1726$ K) were 0.29, 0.34, and 0.40. The homologous temperature at 573 K for the Ni–37%Co, Ni–52%Co, and Ni–74%Co electrodeposits is $\sim$0.33. The driving force for grain growth can be expressed as $P = \alpha\gamma/d$ where α is a grain shape factor (for tetrakaidekahedra $\alpha = 2.37$ [24]), γ is the excess interfacial free energy, and d is the grain size. Taking an extrapolated value for the excess interfacial free energy of Ni ($\gamma = 1.0$ J/m^2 [25]) and the starting grain size ($d = 20$ nm), gives an estimated driving force for grain growth on the order of 1.2×10^8 J/m^3. Note that the driving force of grain growth in the Ni–Co electrodeposits is expected to be on the same order of magnitude.

Curvature-driven bicrystal studies typically have relatively low driving forces for grain boundary migration, on the order of 10^2–10^3 J/m^3 [21, 22], which is up to six orders of magnitude lower than the driving force in the present study. Note that despite the higher driving force, the largest time-averaged AGF velocity measured in this study ($v_{AGF} \approx 36$ nm/s at the start of abnormal grain growth for the largest growing grains in nanocrystalline Ni at 593 K) are still much lower than the grain boundary migration rates typically seen in conventional bicrystal studies. For example, grain boundary velocities of up to 1×10^5 nm/s have been measured in Pb [26] and Al [27] bicrystal studies. However, those studies were conducted at much higher homologous temperatures, 0.79–0.99 [26] and 0.81–0.91 [27]. A more direct comparison can be made to studies of heavily deformed single crystals undergoing recrystallization. These typically have a much higher driving force, on the order of 10^5–10^7 J/m^3 [21, 22], and are generally conducted at lower homologous temperatures, e.g., 0.25–0.45 [21]. Furthermore, like abnormal grain growth, recrystallization is a discontinuous solid state reaction which lowers the microstructural defect density (i.e., of grain boundaries or dislocations, respectively) via a reaction front (i.e., a migrating grain boundary) that separates the transformed and untransformed regions.

The largest of the time-averaged and the overall transformation-averaged interfacial velocities (normalized by their respective driving forces for grain growth) are plotted in Fig. 10 as a function of the homologous annealing temperature. Also shown in Fig. 10 are previously reported grain boundary velocities from recrystallization studies that are plotted over the homologous temperature range at which the measurements were made [28–32]. There are several things to note. First, the normalized grain boundary velocities during recrystallization in zone-refined materials [28–30], having for example a purity of 99.9999% or better [28], is much higher than even the largest of the normalized time-averaged interfacial velocities measured in the present

Fig. 8 Largest abnormally grown grain size class, L_x, as a function of isothermal annealing time at 573 K for the nanocrystalline Ni–37%Co (**a**), Ni–52%Co (**b**), and Ni–74%Co (**c**) electrodeposits

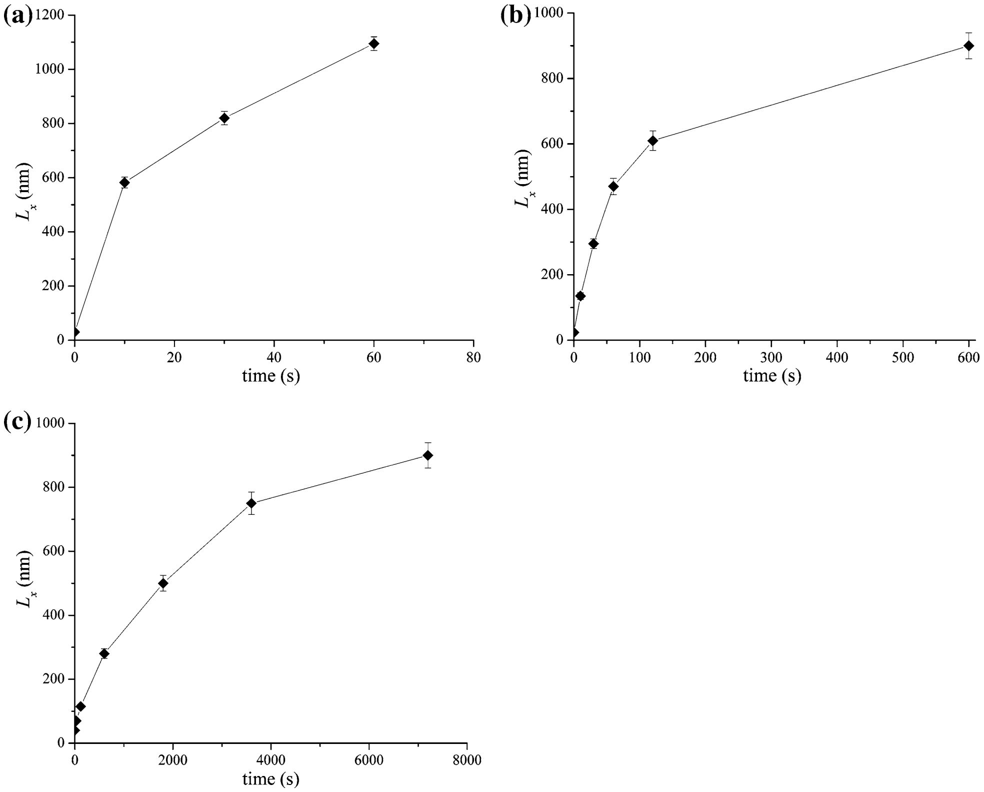

Fig. 9 Time-averaged abnormal growth front velocity (v_{AGF}) as a function of isothermal annealing time at 573 K for the nanocrystalline Ni–37%Co (**a**), Ni–52%Co (**b**), and Ni–74%Co (**c**) electrodeposits

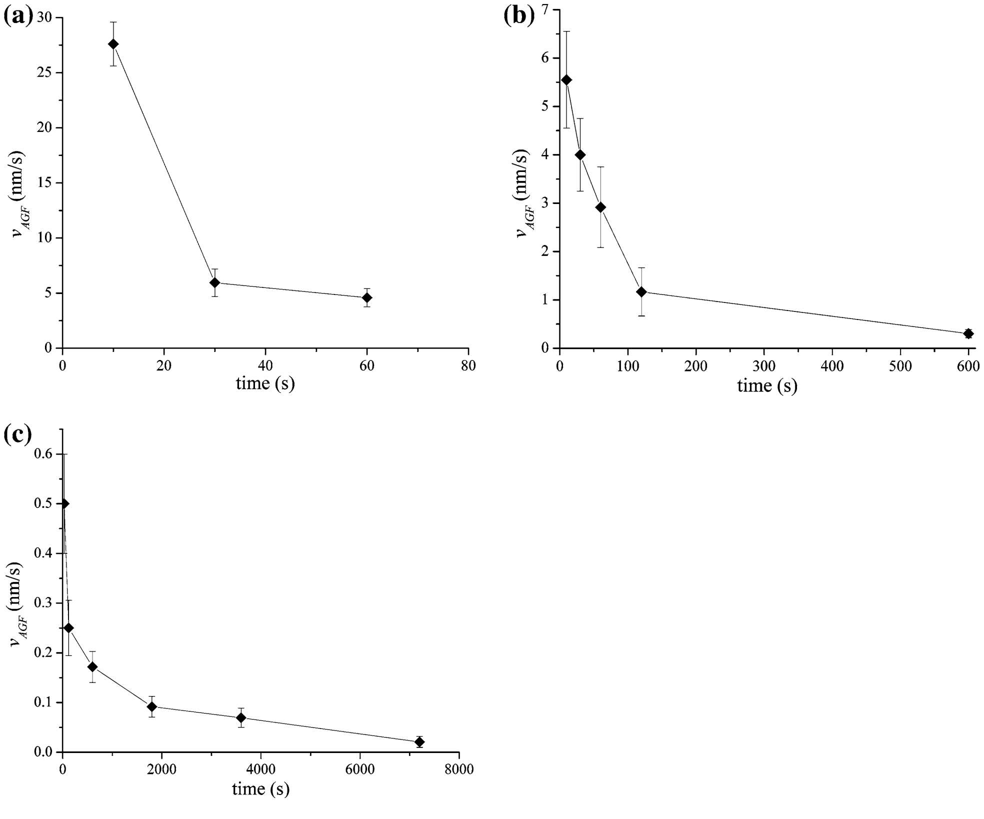

study. At a homologous annealing temperature of 0.33, the normalized recrystallization velocities range from 7.39 × 10^{-15} m^4/J s [30] to 1.36 × 10^{-12} m^4/J s [29]. In contrast, the largest time-averaged AGF velocity at 0.33 T_m was observed in the nanocrystalline Ni–37%Co electrodeposit, with largest abnormally growing grains

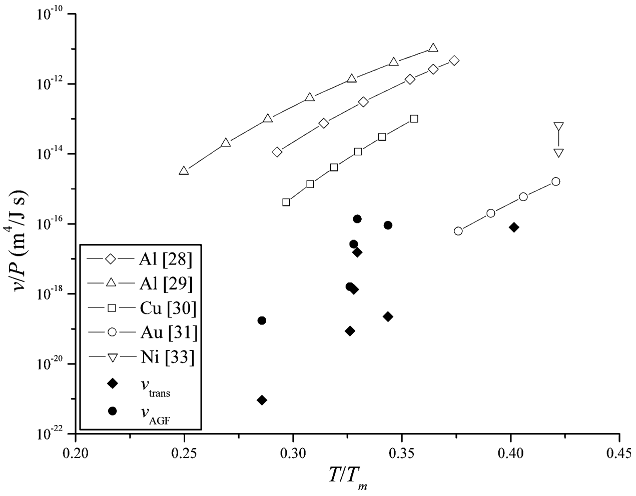

Fig. 10 Experimentally measured grain boundary velocities, v, normalized by the driving force, P, as a function of homologous temperature T/T_m for data from the present study and previous recrystallization studies [28–31, 33]

having normalized upper velocities in the range of 1.38×10^{-16}–4.45×10^{-17} m^4/J s. Furthermore, these were the fastest migrating AGFs (i.e., of the largest grains) and most AGFs are migrating at a much slower rate.

However, there are instances where the normalized recrystallization velocities are comparable to the results of the present study. For example, the normalized grain boundary velocity for recrystallization in a study of 97% rolled gold single crystals [31] containing 20 ppm Fe is plotted in Fig. 10. At annealing temperatures below 290 °C (0.42 T_m) grain boundary migration was controlled by solute drag and the resulting normalized velocities overlap the measured values of the present study. In addition, a recent study of recrystallization in a single phase Al–0.05 wt.% Si alloy measured the grain boundary velocity over the temperature range of 295–400 °C. Grain boundary mobilities were determined from the slope of boundary velocity plotted as a function of driving pressure; an activation energy of $Q = 147$ kJ/mol (with a pre-exponential constant of $M_o = 1.78 \times 10^8$ m^4/J s) was found and it was concluded that the recrystallization kinetics were solute diffusion controlled [32]. While it can be difficult to meaningfully compare grain boundary mobilities measured in different temperature regimes, an extrapolated value for the mobility in Al–0.05 wt.% Si [32] down to a homologous temperature of 0.33 T_m gives a value of 5×10^{-17} m^4/J s, which is comparable to the normalized velocities seen in the present study.

Perhaps the most direct comparison can be made to a recent study of recrystallization in cold-rolled Ni at 728 K having 0.5 ppm S impurities [33]. The driving forces for grain boundary migration ranged from 2.3×10^6 to 11.3×10^6 J/m^3; when the driving force exceeded $\sim 7 \times 10^6$ J/m^3, the boundary was able to break free from the sulfur impurities resulting in a grain boundary velocity of 730 nm/s. At lower driving forces when the sulfur was attached to the boundaries, the grain boundary velocity was below 30 nm/s, which is comparable to the velocities seen in the present study. It is interesting to note that while the driving force for grain boundary migration in the present study of nanocrystalline Ni is approximately 10–50 times higher than those in the recrystallization study of Ni [33], the total sulfur impurity concentration is approximately 1700 times higher for the nanocrystalline case.

Dragging forces

It is worth restating that both velocity parameters in the present study are time-averaged migration rates. In addition, these velocities are significantly lower than the instantaneous interfacial velocities measured during in-situ TEM annealing of the same Ni electrodeposit [7]. The characterization approach in [7] showed that migration occurred in discontinuous steps over limited sections of the AGF. It is interesting to note that there is recent evidence from three-dimensional XRD microscopy indicating that grain boundary migration during recrystallization of commercial purity aluminum occurs by abrupt movement of individual boundary segments [34]. Figure 11 shows an example of the boundary velocity profile for the early stages of one nonuniformly growing grain during the in-situ TEM annealing of nanocrystalline Ni; migration occurred through a series of rapid migration events (of up

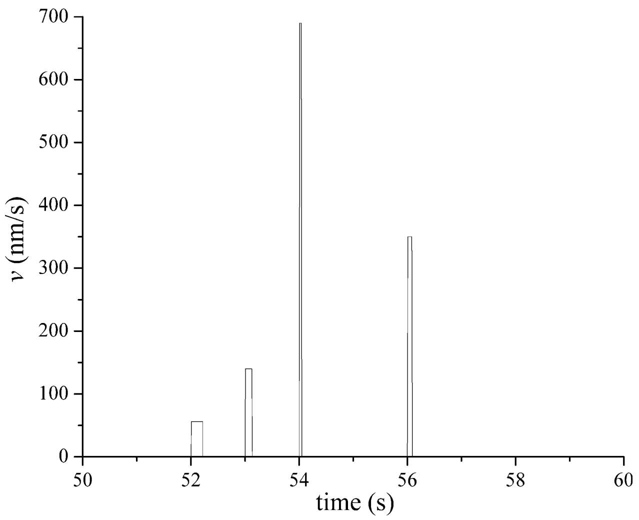

Fig. 11 Velocity profile of nanocrystalline Ni during in-situ TEM annealing giving the estimated instantaneous AGF boundary segment velocity as a function of annealing time at ~681 K [7]. The v_{AGF} parameter of the present study would correspond to a time-weighted average of the discrete boundary migration steps

to 700 nm/s) followed by periods of stagnation [7]. Note that the most rapid boundary segment velocities may have been higher since the temporal resolution was limited to successive video frames (at 0.033 s intervals) and the most rapid events occurred from one frame to the next. This would put the normalized boundary segment velocity closer to the values that are typically seen during recrystallization in high purity materials (e.g., [28–30]). In other words, while the overall time-averaged migration rates for the fastest grains are comparable to the cases of solute-controlled recrystallization, the instantaneous velocity rates may approach what is seen in higher purity materials. Local transformation events of this type are obviously not accessible from the temporally frozen microstructures obtained after ex-situ annealing, and the v_{AGF} parameter of the present study would represent a time-weighted average of the discrete boundary segment migration steps.

For abnormal grain growth into an otherwise stable nanocrystalline matrix (Fig. 4b), the curvature-based driving force would be essentially constant [35]. In other words, the rate of growth would be nearly constant until AGF impingement. The fact that this is *not* observed during the earliest stages of abnormal grain growth indicates that the mobility decreases as the growth fronts advance through the nanocrystalline matrix. The relatively high sulfur concentration in the nanocrystalline matrix (190–850 ppm, Table 1) may explain both the locally discontinuous AGF migration observed by in-situ TEM annealing [7] and the time-averaged AGF velocity with increasing migration distance measured in the present study. Sulfur impurities could act as a dragging force through either or both of solute drag [36, 37] or Zener drag (C. Zener quoted in [38]). There is strong grain boundary segregation potential for sulfur in nickel. Enrichment factors (i.e., $\varepsilon = [\mathrm{S}]_{\mathrm{GB}}/[\mathrm{S}]_{\mathrm{B}}$, where $[\mathrm{S}]_{\mathrm{GB}}$ is the grain boundary sulfur concentration and $[\mathrm{S}]_{\mathrm{B}}$ is the bulk sulfur concentration) on the order of 2×10^4 [39] to 2×10^5 [40] have been reported. To act as a rate-limiting mechanism, sulfur would need to accumulate at the AGFs. At 693 K, the bulk diffusion coefficient of S in Ni is $D = 4.3 \times 10^{-21}\ \mathrm{m}^2/\mathrm{s}$ [41]; the characteristic diffusion length, $\langle x \rangle = \sqrt{Dt}$, of S in the time required to consume the nanocrystalline Ni matrix at 693 K ($t = 30$ s, Table 2) is only $\sim$0.4 nm, i.e., comparable to the grain boundary width. Therefore, relatively little bulk sulfur diffusion would be expected for the annealing conditions of this experiment.

However, solute collection at migrating grain boundaries [42–44] can lead to a diffusion mechanism which bypasses the bulk diffusion process. Indeed, an accelerated segregation mechanism for sulfur in nickel was reported [45], and was later attributed to the collection of sulfur by migrating grain boundaries during recrystallization [46]. This process of grain boundary migration-assisted sulfur segregation during the recrystallization of cold-worked nickel has been reported to be 10^3–10^6 times faster than segregation through bulk diffusion [47]. Furthermore, there is experimental evidence suggesting that sulfur is collected at the migrating AGFs in nanocrystalline nickel during annealing. Klement et al. [1] observed sulfur enrichment at the interface between abnormally grown grains and the surrounding nanocrystalline matrix for a nickel electrodeposit annealed at 493 K for 1800 s. Similar observations were made in a three-dimensional atom probe (3DAP) study of 16 nm starting grain size nickel that was annealed at 523 K for 1 h [48]. Moreover, a study on the effect of starting nanostructure on the thermal stability of nanostructured cobalt found that the sulfur impurity concentration (in the range of 240–980 ppm) was the most important parameter in determining the thermal stability: the peak temperatures of grain growth and the activation energies of grain growth each increased with increasing bulk sulfur concentration [49].

A dynamic sulfur segregation mechanism may be able to explain both the time-averaged interfacial velocity measurements of the present study and the intermittent grain boundary migration seen by in-situ TEM annealing [7]. Once a critical amount of sulfur is accumulated at the migrating AGF, growth may be temporarily halted at which point precipitation of nickel sulfides could occur, which would reduce the local pinning force [50], allowing migration to be reinitiated. There is some experimental evidence to support this interpretation. The as-received selected area electron diffraction patterns exhibited only the Ni (FCC) diffraction rings [4–7], while annealed nanostructures exhibited both Ni (FCC) rings and extra diffraction spots corresponding to second phase precipitates. A typical example is shown in Fig. 12 for a nanocrystalline Ni electrodeposit that had been isothermally annealed at 493 K for 3600 s. Note that the second phase particles were too small to be directly observed in the contrast-rich annealed nanostructures. However, the interplanar spacing corresponding to the diffracting planes of the extra diffraction spots within the first Ni (111) ring were calculated by measuring their radial distance from the directly transmitted (000) beam. While it was difficult to unambiguously index all additional diffraction spots, some of the measured interplanar spacings can be accounted for by $\mathrm{Ni_3S_2}$ precipitates.

Finally, it is interesting to compare the results of this study to those from an in-situ TEM annealing study of abnormal grain growth in pulse-laser deposited nanocrystalline Ni [51]. Grain boundary velocities of 5.5×10^{-3}–60 nm/s were reported over the homologous temperature range of 0.29–0.39 [51]. These values are comparable in magnitude to the transformation-averaged velocities of the present study (Table 2) and were conducted over

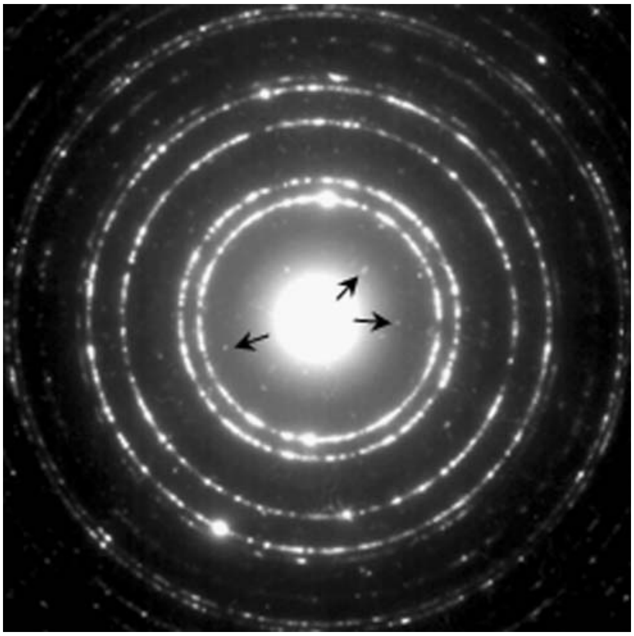

Fig. 12 Typical selected area electron diffraction pattern of electrodeposited nanocrystalline Ni after 3600 s of isothermal annealing at 693 K; arrows indicate examples of extra diffraction spots observed in addition to the Ni (FCC) diffraction rings

essentially the same temperature range (0.29–0.40 T_m). Similar to the present study, it is possible that a dynamic solute drag mechanism might be a contributing factor to the comparatively low grain boundary velocities reported in the pulse-laser deposited Ni. While impurity values were not specifically reported in that in-situ TEM annealing study [51], Rutherford backscattering spectrometry of pulse-laser deposited Ni from a related study reported O contamination values of up to 1.4 wt.% [52]. In electrodeposited nanocrystalline Ni, oxygen impurities on the order of 0.6 wt.% (deliberately introduced by applying a reversing pulse during deposition) were found to significantly increase the thermal stability with no measurable grain growth below 623 K and only limited growth from 19 to 35 nm after 150 min at 673 K [53]. Unlike the present study, however, the formation of second phase precipitates was not reported in pulse-laser deposited Ni after abnormal grain growth; instead, stacking fault tetrahedra were seen in the wake of the migrating AGFs [51]. These defect structures have not been seen in previous grain growth studies of nanocrystalline Ni electrodeposits (e.g., [1, 2]) and were not seen in the present study. Stacking fault tetrahedra formation was attributed to the elimination of excess volume associated with the annihilated grain boundaries [51]. It has been suggested that vacancies can act as a dragging force [54] and their effect might become important for the smallest grain size nanocrystalline materials when the excess volume associated with the grain boundaries becomes significant [55]. Indeed, the intercrystalline volume fraction associated with the smaller starting grain size of the pulse-deposited nanocrystalline Ni (6 nm [51]), would be approximately three times larger than that of the 20 nm starting grain size Ni of the present study [56].

Conclusions

Two velocity parameters were developed to quantify the interfacial migration rates in nanocrystalline materials, an overall transformation-averaged parameter and the time-averaged AGF velocity of the most rapidly growing grains. The temperature dependence of the transformation-averaged grain boundary velocity is consistent with the activation energy of grain growth measured by calorimetry. Furthermore, the interfacial velocity is strongly dependent on the thermal stability of the particular electrodeposit—a difference in calorimetric peak temperature range of 35 K leads to nearly two orders of magnitude difference in transformation-averaged interfacial velocity. Despite the rapid loss of nanostructure at elevated temperatures, the time-average AGF velocities in nanocrystalline electrodeposits are several orders of magnitude lower than the normalized grain boundary velocities reported during recrystallization in high purity systems. Furthermore, the grain boundary velocity decreases with increasing migration distance. These observations can be interpreted in terms of a dynamic sulfur segregation model, in which the migrating AGFs collect sulfur as they migrate through the nanocrystalline matrix.

Acknowledgements Financial support from the Natural Sciences and Engineering Research Council of Canada (NSERC) and nanocrystalline Ni and Ni–Co samples from Integran Technologies Inc. of Toronto, Canada are gratefully acknowledged.

References

1. Klement U, Erb U, El-Sherik AM et al (1995) Mater Sci Eng A 203:177. doi:10.1016/0921-5093(95)09864-X
2. Wang N, Wang Z, Aust KT et al (1997) Acta Mater 45:1655. doi:10.1016/S1359-6454(96)00254-6
3. Natter H, Schmelzer M, Hemplemann R (1998) J Mater Res 13:1186. doi:10.1557/JMR.1998.0169
4. Hibbard GD, Erb U, Aust KT et al (2000) Mater Res Soc Symp Proc 580:183
5. Hibbard GD, Erb U, Aust KT et al (2002) Mater Sci Forum 386–388:387
6. Hibbard GD, Aust KT, Palumbo G et al (2001) Scr Mater 44:513. doi:10.1016/S1359-6462(00)00628-X
7. Hibbard GD, Radmilovic V, Aust KT et al (2008) Mater Sci Eng A 494:232. doi:10.1016/j.msea.2008.04.054
8. Cheng L, Hibbard GD (2008) Mater Sci Eng A. doi:10.1016/j.msea.2008.03.025

9. Kim BK, Szpunar JA, Varano R (2002) Mater Sci Forum 408–412:937
10. Seo JH, Kim JK, Yim TH et al (2005) Mater Sci Forum 475–479:3483
11. Klement U, da Silva M (2007) J Alloys Comp 434–435:714
12. Lee SB, Hwang NM, Yoon DY, Henry MF (2000) Met Mater Trans A 31:985
13. Czerwinski F, Li H, Megret M et al (1997) Scripta Mater 37:1967
14. Park YB, Park J, Ha CS et al (2002) Mater Sci Forum 408–412:919
15. Kim JK, Seo JH, Park YB (2004) Mater Sci Forum 467–470:1313
16. Hibbard GD, Aust KT, Erb U (2006) Mater Sci Eng A 433:195
17. Erb U, El-Sherik AM (1994) US Patent 5353266
18. Erb U, El-Sherik AM, Cheung CKS et al (1995) US Patent 5433797
19. El-Sherik AM, Erb U (1995) J Mater Sci 30:5743
20. Chen LC, Spaepen F (1991) J Appl Phys 69:679
21. Haessner F, Hofman S (1978) In: Haessner F (ed) Recrystallization of metallic materials. Riederer Verlag, Stuttgart
22. Gottstein G, Shvindlerman LS (1999) Grain boundary migration in metals. CRC Press, New York
23. Humphreys FJ, Hatherley M (2004) Recrystallization and related annealing phenomena. Elsevier, Oxford
24. DeHoff RT, Rhines FN (1968) Quantitative microscopy. McGraw-Hill, New York
25. Murr LE (1975) Interfacial phenomena in metals and alloys. Addison-Wesley, Don Mills, Canada
26. Aust KT, Rutter JW (1959) Trans AIME 215:119
27. Shvindlerman LS, Gottstein G, Molodov DA (1997) Phys Stat Sol A 160:419
28. Gordon P, Vandermeer RA (1962) Trans AIME 224:917
29. Fromageau R (1969) Mem Sci Rev Metall 66:287
30. Haessner F, Holzer HP (1974) Acta Met 22:695
31. Grunwald W, Haessner F (1970) Acta Metall 18:217
32. Huang Y, Humphreys FJ (1999) Acta Mater 47:2259
33. LeGall R, Liao G, Saindrenan G (1999) Scripta Mater 41:427
34. Schmidt S, Nielsen SF, Gundlach C et al (2004) Science 305:229
35. Burke JE, Turnbull D (1952) Prog Metal Phys 3:220
36. Cahn JW (1962) Acta Met 10:789
37. Lucke K, Stuwe HP (1963) In: Himmel L (ed) Recovery and recrystallization of metals. Wiley, New York
38. Smith CS (1948) Trans AIME 175:15
39. Pierantoni M, Aufray B, Cabane F (1985) Acta Met 33:1625
40. Bruemmer SM, Jones RJ, Thomas MT et al (1981) In: Louthan MR, McNitt RP, Sisson RD Jr (eds) Environmental degradation of engineering materials in aggressive environments. Virgina Tech Printing, Blacksburg, VA
41. Beaunier L, Chefi C, Froment M et al (1981) Mem Sci Rev Metall 78:417
42. Aust KT, Rutter JW (1962) In: Ultra high purity metals. ASM, Metals Park OH
43. Roeder E, Klerk M (1963) Z Metallkde 54:462
44. Hook RE, Garrett HJ, Adair AM (1963) Trans AIME 227:145
45. Barbier-Vitart J, Saindrenan G, Larere A (1982) J Mater Sci 17:387
46. Saindrenan G, Larere A (1984) Scripta Met 18:969
47. Le Gall R, Saindrenan G, Roptin D (1992) Scripta Mater 26:1291
48. Thuvander M, Abraham M, Cerezo A et al (2001) Mater Sci Tech 17:961
49. Hibbard GD, Aust KT, Erb U (2006) Acta Mater 54:2501
50. Mehta SC, Smith DA, Erb U (1995) Mater Sci Eng A 204:227
51. Hatter K, Follstaedt DM, Knapp JA, Robertson IM (2008) Acta Mater 56:794
52. Knapp JA, Follstaedt DM (2004) J Mater Res 19:218
53. Natter H, Loffler MS, Krill CE, Hempelmann R (2001) Scripta Mater 44:2321
54. Gleiter H (1979) Acta Metall 27:187
55. Estrin Y, Gottstein G, Shvindlerman LS (1999) Scripta Mater 41:385
56. Palumbo G, Thorpe SJ, Aust KT (1990) Script Metall 24:1347